Significant Radiation Tolerance and Moderate Reduction in Thermal Transport of a Tungsten Nanofilm by Inserting Monolayer Graphene

Shuyao Si, Wenqing Li, Xiaolong Zhao, Meng Han, Yanan Yue, Wei Wu, Shishang Guo, Xingang Zhang, Zhigao Dai, Xinwei Wang, Xiangheng Xiao,* and Changzhong Jiang*

Energy source is an important material basis for the survival and development of all humans. In order to meet today's ever-increasing demand for energy, various energy technologies have been developed among which nuclear energy is the most effective option that has enormously attracted researchers' attention.[1] Nowadays, a concept known as "nuclear prosperity" is becoming the talk of the public. To design an environmentally friendly and advanced nuclear power system has been a matter of great urgency.[2] However, in a variety of harsh environments of nuclear reactors which contain neutron radiation, the large quantity and high energy helium ions induced by transmutation can swiftly combine with vacancies to form He bubbles.[3] The appearance of He bubbles strengthens embrittlement and swelling, which can even bring about complete failure of materials, especially structural materials and closer plasma-facing materials.[4] Meanwhile, if heat cannot be removed promptly from the core during nuclear reaction, the fuel cladding will lead to disastrous and irreparable consequences.[5] For example, on March 11, 2011, the reactor decay heat failed to be transported (Loss-of-Coolant Accident) in time during a tsunami, which was directly responsible for the catastrophic Fukushima Nuclear Accident.[6] Therefore, it is necessary to search for a suitable material with both excellent radiation tolerance and wonderful thermal properties in order to address the technological challenges.[1,7] Indeed, the safety of fission and fusion substantially depends on the performance of such a material.[8,9] For all researchers in this field, it is urgent to enhance, by regulating the behaviors of radiation damage in structural materials, the radiation tolerance (including thermal properties) for the purpose of extending the service life of nuclear reactors.

Concerning radiation tolerance, it is widely accepted that a variety of interfaces in composite materials can provide sinks for defects from radiation, and thus enhance the radiation tolerance.[10,11] Therefore, a great number of composite materials designed to contain period multilayer interfaces have been studied in detail over the last several decades.[12,13] For instance, in metallic multilayer system, W/Cu,[14,15] Cu/Nb,[16,17] and Cu/V,[18,19] as well as coherent or incoherent Cu/Fe[20] interfaces have been studied clearly and thoroughly. And more recently, Kim et al.[21] analyzed, with the help of an in situ SEM nanopillar compression testing, the capabilities of V-graphene nanolayered composites in terms of reduction in radiation-induced hardening and suppression of brittle failure.

However, owing to the thermal boundary resistance,[22] the cladding designed for bi-metal multilayer systems could more seriously decrease thermal conductivity than pure constituents do. Up to now, little importance has been attached to how to improve heat conduction of multilayer composites. It is critical, however, for the cladding to act simultaneously as a conductor that can efficiently transfer nuclear heat from fuel to the coolant.[8] Furthermore, as an advanced material with attractive thermal properties which have been scrutinized in various fields,[23–25] graphene (G) has barely been applied in radiation tolerance. In fact, because of its impermeability to all standard gases (including He gas),[26] graphene is regarded as an effective material in retarding the radiation damage.[21] In addition, high-quality graphene has been produced on an industrial scale.[27,28] Equally important, tungsten (W), a metal with relatively high melting points, high thermal conductivity and excellent radiation tolerance, has been widely researched.[14,29] Tungsten matrix materials are the most promising candidate for plasma facing materials like first-wall materials in future fusion reactors, which have seen significant progress in recent researches.[29–32] All of these factors have contributed to the motivation for this work.

Dr. S. Si, Dr. W. Li, Dr. X. Zhao, Prof. S. Guo, Dr. X. Zhang, Prof. X. Xiao, Prof. C. Jiang
Department of Physics and Key Laboratory of Artificial Micro- and Nanostructures of Ministry of Education
Hubei Nuclear Solid Physics Key Laboratory and Center for Ion Beam Application
Wuhan University
Wuhan 430072, P. R. China
E-mail: xxh@whu.edu.cn

Dr. M. Han, Prof. X. Wang
Department of Mechanical Engineering
Iowa State University
Ames, IA 50010, USA
E-mail: xwang3@iastate.edu

Prof. Y. Yue
School of Power and Mechanical Engineering
Wuhan University
Wuhan, Hubei 430072, China

Prof. W. Wu, Dr. Z. Dai
Laboratory of Printable Functional Nanomaterials and Printed Electronics
School of Printing and Packaging
Wuhan University
Wuhan 430072, P. R. China

DOI: 10.1002/adma.201604623

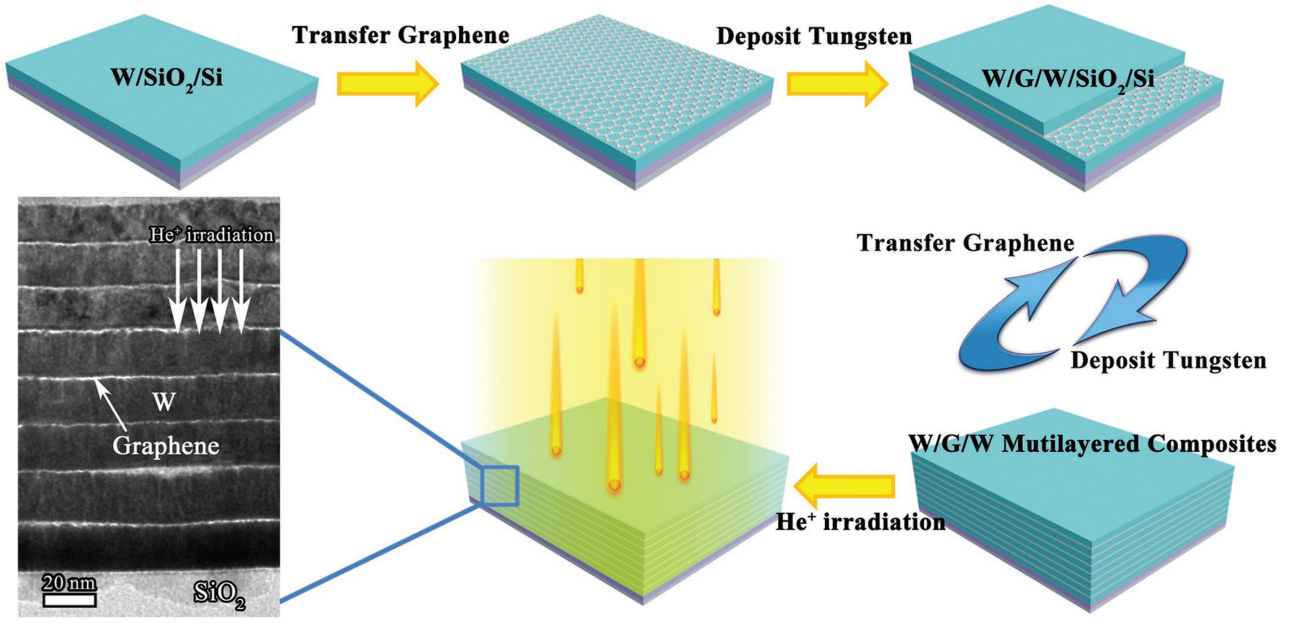

Figure 1. Schematic of tungsten–graphene multilayer system fabrication and process of He^+ ion irradiation. The TEM is W/G nanofilm with 15 nm period-thickness irradiated by 50 keV He^+ ions to a fluence of 1×10^{17} ions cm^{-2}.

In the present paper, we use a stacking method to fabricate W–G multilayer composites (W/G) and W–W multilayer composites (W/W), as well as pure W control. The property of thermal resistance induced by graphene layers sandwiched in tungsten films is investigated by using a photothermal (PT) technique.[33–35] Then, based on the stopping and range of ions in matter (SRIM) computer program used to calculate displacement per atom (DPA) and He concentration,[36,37] helium-ion-beam irradiation is performed to simulate neutron irradiation. Transmission electron microscopy (TEM) is used to characterize the radiation damage (including that of interfaces and He bubbles). The interface thermal resistance between monolayer graphene and tungsten nanofilms is not greater than 1.8×10^{-8} K m^2 W^{-1}, which proves that our W-graphene multilayer composites can efficiently transfer nuclear heat and effectively alleviate radiation damage as expected.

Figure 1 schematically illustrates the fabrication and He-ion-implantation process. Monolayer graphene was transferred onto the W film sputtered on Si/SiO_2 substrate. Optical imaging and Raman spectroscopy reveal that the transferred graphene is intact and high-quality monolayer graphene (Figure S2, Supporting Information). Then, the next same-thickness W nanofilm layer was deposited on top of the graphene. By repeating the above process, the W/G multilayer films could be obtained (Figure 1).

To adequately characterize the thermal transport across thin films to obtain thermal resistance induced by graphene inclusions, we have, respectively, prepared 3L(W/G), 5L(W/G), and 7L(W/G) nanofilms (where numerals represent numbers of cycles of G transferring and W sputtering) and corresponding control samples without graphene. Also, each multilayer nanofilm sample has three tungsten period-thicknesses of 15, 30, and 40 nm; a group of single-layer pure tungsten nanofilms were prepared, which were similar to corresponding multilayer nanofilms in total thicknesses (all samples prepared are given in Table S1, Supporting Information). Figure S3 (Supporting Information) shows SEM images of $3L(W_{40}/G)$, $5L(W_{40}/G)$, $7L(W_{40}/G)$, and corresponding single-layer pure tungsten films (subscripts represent period-thicknesses). In this characterization, a PT technique is used to characterize thermal transport across thin films.

Figure 2a schematically shows the arrangement and operation for measuring thermal properties. Typically, a square-wave-modulated laser beam is used to heat the material, which

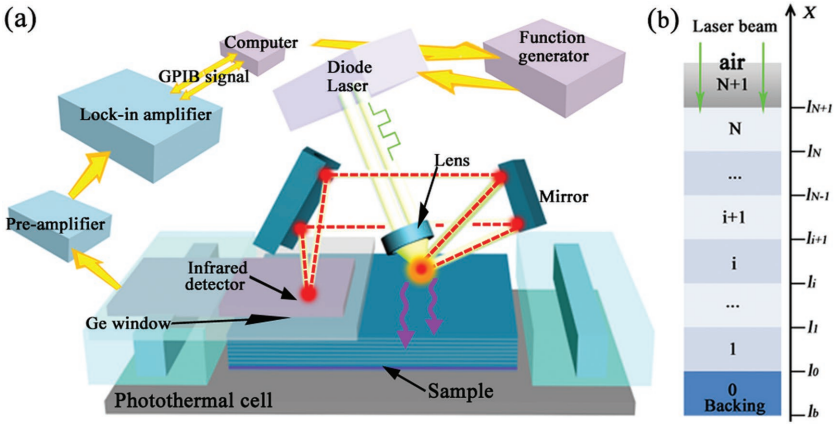

Figure 2. a) Schematic of the experimental setup for characterizing the thermal resistance. b) Schematic of an N-layer sample, which shows a multilayer 1D heat transfer model.

induces thermal radiation from the sample's surface and it is related to the modulated laser frequency and thermal properties of the film. After the thermal radiation signals within a large range of modulated laser frequency are obtained, thermal transport properties of the sample can be determined. There is a Ge window placed in front of the infrared detector with the purpose of filtering out the reflected laser beam and allowing only the thermal radiation to pass. In this experiment, the laser frequency ranges from 600 to 20000 Hz, within which the thermal diffusion length in the sample is much smaller than the spot size. In this case, the experiment can be simplified as a 1D cross-plane heat-transfer model. Figure 2b shows a cross-sectional view of this model. For the thermal diffusion in layer i the 1D governing equation can be expressed as:

$$\frac{\partial^2 \theta_i}{\partial x^2} = \frac{1}{\alpha_i}\frac{\partial \theta_i}{\partial t} - \frac{\beta_i I_0}{2k_i}\exp\left(\sum_{m=i+1}^{N} -\beta_m L_m\right) \times e^{\beta_i (x-l_i)}\left(1+e^{j\omega t}\right) \quad (1)$$

In this model, physical properties of layer i such as thickness $L_i = l_i - l_{i-1}$, thermal conductivity k_i, specific heat $c_{p,i}$, thermal diffusivity α_i, and optical absorption coefficient β_i are needed. Other parameters in this model are the modulated laser frequency f, the thermal diffusion coefficient a_i, and the thermal contact resistance $R_{i,i+1}$ between layer i and i+1. Details of the solution to this model can be seen in the report by Hu et al.[38]

Here in this experiment, the unknown parameters are thermal conductivity (k) of W nanofilm and thermal contact resistance ($R_{W/G}$) induced by graphene. With other parameters fixed, trial value of k and $R_{W/G}$ is used to calculate the theoretical phase shift at every modulated laser frequency. Thermal characterization results are obtained from the fitting of theoretical phase shifts. From the fitting process of the single-layer tungsten and multilayer tungsten samples, the thermal conductivity of the tungsten film is determined at 2.05 W m^{-1} K^{-1}. Thermal resistance induced by the graphene layers of each sample is calculated, and detailed results are summarized in **Table 1**.

It is seen from Table 1 that the graphene-induced thermal resistance varies from sample to sample. This is due to the sample preparation as the graphene layers are transferred to the tungsten films manually. However, it should be noticed that, thermal resistance induced by the graphene layer is no greater than 1.8×10^{-8} K m^2 W^{-1} (maximum at 1.792×10^{-8} K m^2 W^{-1} for sample 5L(W_{40}/G)). This value is comparable with the graphene/SiO_2 interface resistance (ranging from 5.6×10^{-9} to 1.2×10^{-8} K m^2 W^{-1} as reported by Chen et al.[39] while much smaller than that of the epitaxial graphene and SiC interface (5.3×10^{-5} K m^2 W^{-1} as reported by Yue et al.[40]). The corresponding thermal conductance is 55 MW m^{-2} K^{-1}, which is also comparable with that of the graphene/SiO_2 interface (ranging from 20 to 110 MW m^{-2} K^{-1} as reported by Mak et al.[41]) and that of the Au/Ti/graphene/SiO_2 interface (about 25 MW m^{-2} K^{-1} as reported by Koh et al.[42]). It is also noticed that there are some negative interface thermal resistance values, such as 3L(W_{15}/G) and 3L(W_{30}/G). There could be two reasons: first, the interface resistance between graphene and tungsten for these two samples is too small that little variation in the sample thickness measurement of tungsten thin film could result in this negative value. Another reason could be the direct thermal transport between adjacent tungsten thin films overcomes the resistance induced by multilayer interfaces for these two samples. This phenomenon was previous observed by Zhang et al.[25] In their measurement, they embedded graphene between Al film and Si substrate and found that this configuration might improve interfacial thermal transport, showing an apparently negative thermal contact resistance of graphene interface materials. The reason could be that graphene prevents the diffusion of Al atoms into the substrate and reduces the thickness of the intermixing layer.[43]

Previous work on characterizing thermal transport phenomena in the W/graphene/Cu structure reported a lower thermal conductance (larger thermal resistance ≈4–5 MW m^{-2} K^{-1} by Jagannadham).[44] This is due to the thicker graphene layers and the heating-induced reaction at the W/graphene interface. In his work, thicker graphene platelets (up to 10–15 atomic layers) were sandwiched between tungsten and Cu, which induced significant thermal resistance as graphene has very low thermal conductivity in C-direction,[45] while in the present work, graphene sandwiched in tungsten sublayers is characterized as having just single-layer carbon atoms. Besides, during his measurement process, the sample was heated at 650 and 900 °C, which induced formation of tungsten carbide (WC) at the W/graphene interface leading to separation and formation of voids. This unmatched contact and nanocrystalline WC film also cause significant reduction of the thermal conductance. In contrast, the present experiment is taken in the atmosphere and the laser heating is controlled at very low energy to make sure no reaction or damage occurs at the interfaces. It is also to worth mentioning in the present work that thermal conductivity of the tungsten film and thermal conductance induced by the graphene layers can be determined simultaneously with high accuracy by applying the PT technique to the pure W, multilayer W/W and multilayer W/G nanofilms under the same condition.

To verify the radiation tolerance of W/G multilayer composites, He-ion implantation was applied to generate radiation damage.[46] The samples of 7L(W_n/G)(n = 15, 30, 40), which correspond to different period-thicknesses, are labeled as W_{15}/G, W_{30}/G, and W_{40}/G, respectively. As a control, the same period-thickness multilayer composites without G are labeled W_{15}/W, W_{30}/W, and W_{40}/W, respectively, and pure W films are deposited

Table 1. Thermal resistance induced by graphene layers.

Sample[a)]	$2R_{W/G}$ [$\times 10^{-9}$ K m^2 W^{-1}]
3L(W_{15}/G)	–3.30
5L(W_{15}/G)	8.50
7L(W_{15}/G)	5.13
3L(W_{30}/G)	–0.90
5L(W_{30}/G)	14.78
7L(W_{30}/G)	16.59
3L(W_{40}/G)	9.87
5L(W_{40}/G)	17.92
7L(W_{40}/G)	10.29

[a)]Regular 3, 5, and 7 in each sample represent numbers of cycles of G transferring and W sputtering. The subscripts represent period-thicknesses: 15, 30, and 40 nm.

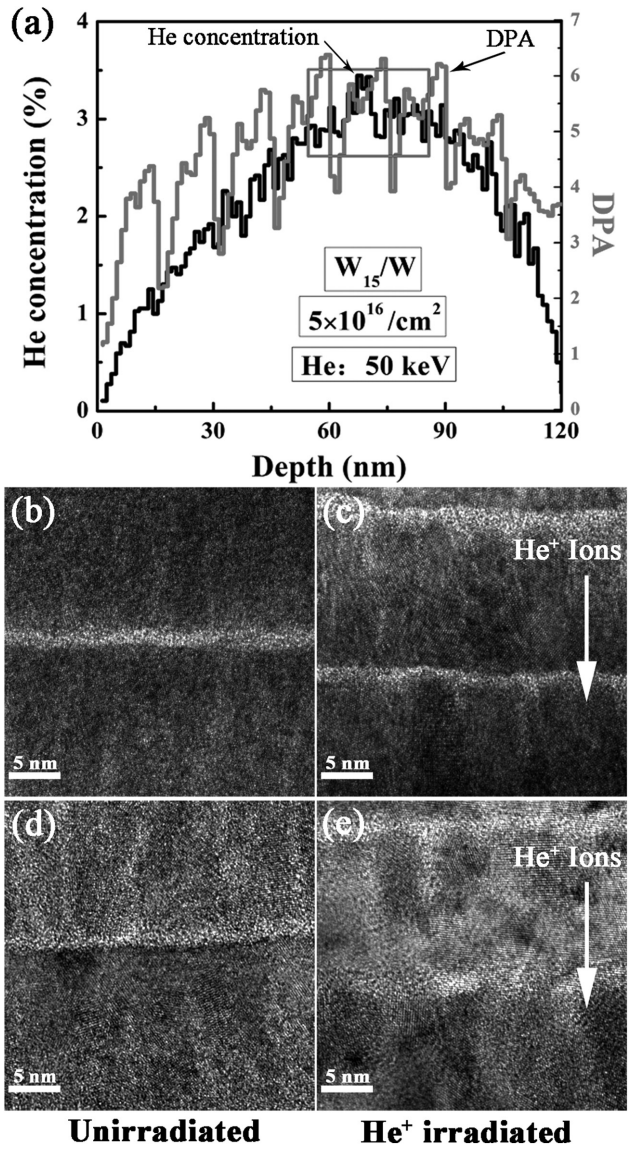

Figure 3. a) SRIM calculations that simulate the variation of He concentration (left) or DPA (right) versus radiation depth in W_{15}/W subjected to He-ion irradiation at 50 keV with a total influence of 5×10^{16} cm^{-2}, the same as the experimental conditions. b–e) TEM images: as-deposited W_{15}/G (b); irradiated W_{15}/G (c); as-deposited W_{15}/W (d); irradiated W_{15}/W (e). All regions of (c) and (e) chosen are from the rectangular box in (a).

as well (see Experimental Section for details). The SRIM computer program is used to calculate DPA and He concentration versus radiation depth, which is same as that in the experimental settings. **Figure 3**a shows the SRIM calculations, which simulate the variation of He concentration (black, left) and DPA (red, right) versus implantation depth in W_{15}/W irradiated by 50 keV He^+ ions to a fluence of 5×10^{16} ions cm^{-2}. SRIM simulation indicates that He concentration is ≈3.5 at% (or 35 000 appm) at a depth of ≈70 nm underneath the film surface and DPA is ≈6.4 at a depth of ≈60 nm. It is worth noting that the locations of peak He-ion concentration of W_{30}/G and W_{40}/G are ≈120 nm and ≈140 nm, respectively (Figure S4a,b, Supporting Information).

TEM images of Figure 3b,d reveal the interface microstructure of as-deposited W_{15}/G and W_{15}/W multilayer composites (left), respectively. In contrast, the peak damage area of W_{15}/G and W_{15}/W irradiated by 50 keV He^+-ion irradiation at room temperature up to a fluence of 5×10^{16} ions cm^{-2} is shown on the right (Figure 3c,e). All areas of the TEM images (Figure 3c,e) chosen are from the rectangular box in Figure 3a. The peak DPA is ≈6.4 at a depth of ≈60 nm underneath the surface. The interface of unirradiated W_{15}/G and W_{15}/W is clearly distinguished. However, after irradiation, the W_{15}/W multilayered sample without graphene becomes unstable (Figure 3e). The original interface showing as Figure 3d appears partially mixed, and some areas even become indistinguishable. Surprisingly, the interface of W_{15}/G subjected to He^+-ion irradiation is still stable (Figure 3c). What these TEM images suggest is that the interface of W_{15}/G appeared discernible after irradiation due to a monolayer graphene embedded between W layers. Although monolayer graphene is just a single layer of carbon atom, the W/G multilayer system can resist radiation damage to some extent due to the role of the W/G interfaces acting as sinks for defects, which is theoretically predicted by Huang et al. with the MD method.[47] Just like traditional bimetallic multilayer nanofilms, the design of metal–graphene multilayer nanofilms is a new strategy for releasing defects and reducing radiation damage.

To give a further demonstration of the radiation tolerance of W/G multilayer system, several nanofilms with period-thicknesses of 15, 30, and 40 nm are irradiated at the same time. **Figure 4**a–c, respectively, show as-deposited W_{15}/G, W_{30}/G, and W_{40}/G multilayer nanofilms. Figure 4d–f, respectively, show peak He concentration region of irradiated W_{15}/G, W_{30}/G, and W_{40}/G multilayered nanofilms by 50 keV He^+ ions up to a fluence of 5×10^{16} ions cm^{-2}. Based on SRIM calculations, the peak He-ion concentration for this experimental condition in the W_n (n = 15, 30, 40)/W structure reaches ≈3.5, ≈4.9, and ≈5.0 at% at depths of ≈60, ≈120, ≈140 nm (Figure S4a,b, Supporting Information). The dashed lines in Figure 4, respectively, represent the locations underneath the film surface. Obviously, for all of the multilayer nanofilms, the interfaces of the peak He-concentration region remain intact and distinguished after irradiation of He^+ ions to a fluence of 5×10^{16} ions cm^{-2} and the interfaces are not mixed because of the presence of graphene discussed above. The Figure 4d, as a whole, appears to show flatter interfaces. However, the interfaces become coarser in this area for W_{30}/G and W_{40}/G multilayer nanofilms (Figure 4e,f). The results show that interface-unevenness tends to increase with period-thickness. Moreover, no detectable bubbles are observed from W_{15}/G and W_{30}/G nanofilms, as compared to W_{40}/G multilayered nanofilms, which form a handful of He bubbles (Figure 4d–f). Figure 4g–i is magnified from the peak He concentration area of Figure 4d–f to explore this phenomenon in detail. For the W/G multilayer nanofilm with 15 nm period-thickness, no agglomerating He bubbles are detected in Figure 4g, which shows the peak He concentration area. The density of He bubbles has a significant positive correlation with the increment of period-thickness. Several He bubbles are sporadically dotted around the W layers and W/G interface. In particular, W layers are a series of columnar crystal, which contains many grain boundaries (Figure S3, Supporting

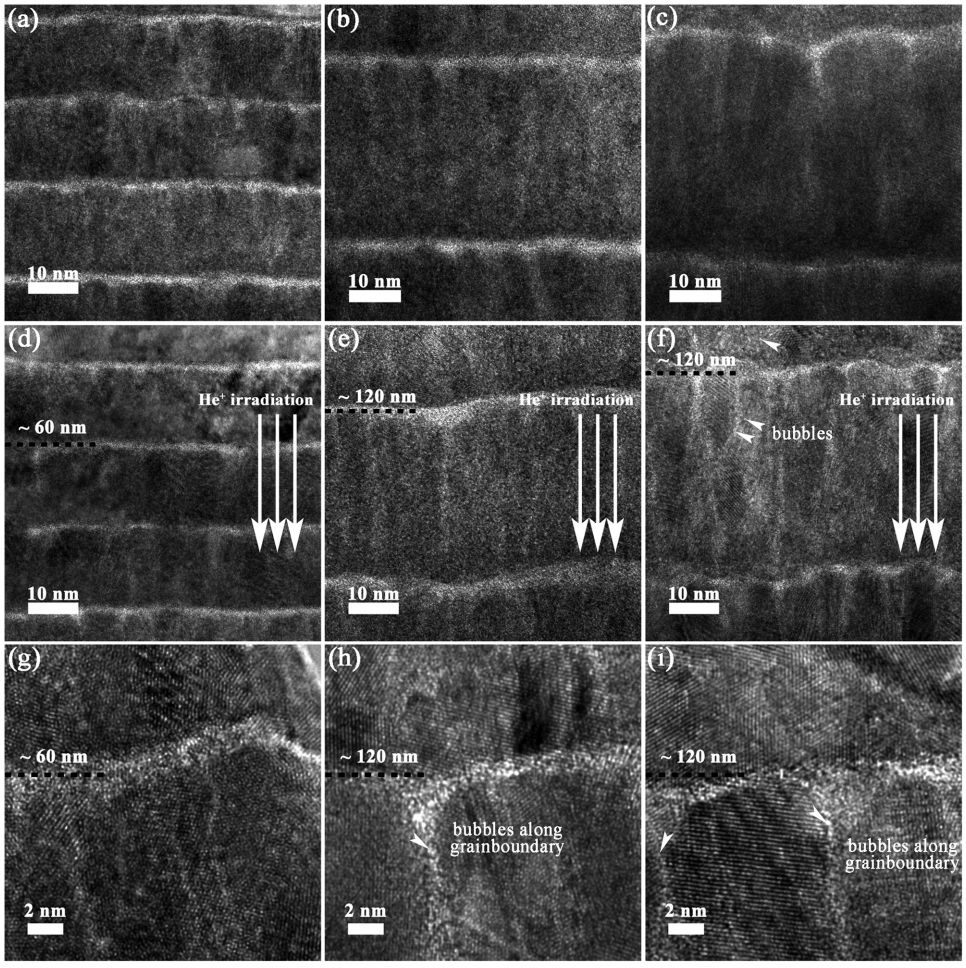

Figure 4. a–c) TEM images: as-deposited W_{15}/G (a); as-deposited W_{30}/G (b); and as-deposited W_{40}/G (c). d–f) TEM images of peak He concentration region under 50 keV He^+ irradiation to a total influence of 5×10^{16} ions cm^2: W_{15}/G (d); W_{30}/G (e); and W_{40}/G (f). g–i) TEM images of peak He concentration region at high magnification: W_{15}/G (g); W_{30}/G (h); and W_{40}/G (i). The dashed lines, respectively, represent the location underneath the film surface. Corresponding SRIM calculation of multilayers with 15 nm period-thickness is shown in Figure 3a. Others are shown in Figures S4a,b (Supporting Information).

Information), and He bubbles appear to align and distribute along these W grain boundaries. In contrast, W grain boundaries are not obviously observed in as-deposited W/G multilayer nanofilms (Figure 4a–c). Surprisingly, a relatively large number of He bubbles seem to preferentially accumulate in these grain boundaries stored to form He nanochannels rather than densely and disorderly accumulate He bubbles or even clusters of He bubbles. Also, all of the He nanochannels extend from the graphene interface along the direction of the irradiation. In Figure 4g, the W_{15}/G nanofilm rarely has He nanochannels. Occasionally, one obscure He nanochannel ≈7 nm length is observed. The length of the He nanochannels in W_{30}/G and W_{40}/G nanofilms is about 11 nm or longer (Figure 4h,i) and the width of He nanochannels tends to slightly increase with period-thickness. The above analysis shows the performance of W_{15}/G appears to be more stable for radiation tolerance, and nanofilms with smaller period-thickness have higher radiation tolerance than those with larger period-thicknesses.

Then, continually increasing the He-ions fluence to 1×10^{17} ions cm^{-2}, we get the panoramic TEM image of the irradiated W_{15}/G nanofilm as shown in Figure 1. TEM images of W_{30}/G and W_{40}/G at this fluence are displayed in Figure S5 (Supporting Information). Meanwhile, an as-deposited pure W nanofilm is shown in **Figure 5**b in comparison to that of the irradiated pure W nanofilm (Figure 5c). Obviously, the W_{15}/G multilayer nanofilm has clear interfaces. No obviously agglomerating He bubbles are observed in each layer. Figure 5b faintly shows a columnar crystal of as-deposited pure W. Unfortunately, dense He bubbles are easily observed everywhere in irradiated pure W nanofilm, though grain boundaries also become preferable places for He bubbles to align and distribute. Furthermore, the average bubble size in the irradiated pure W nanofilm is 0.7 ± 0.2 nm, whereas it is 0.3 ± 0.2 nm in W_{15}/G nanofilm. Also, grain boundaries become preferable places for He bubbles to align and distribute. To further examine radiation tolerance of W_{15}/G nanofilm, magnified TEM images of Figure 1 in different regions are, respectively, displayed in Figure 5d–g for better observation of bubbles and interfaces. Accordingly, the implantation depth dependent He concentration and DPA profile from SRIM calculations are shown

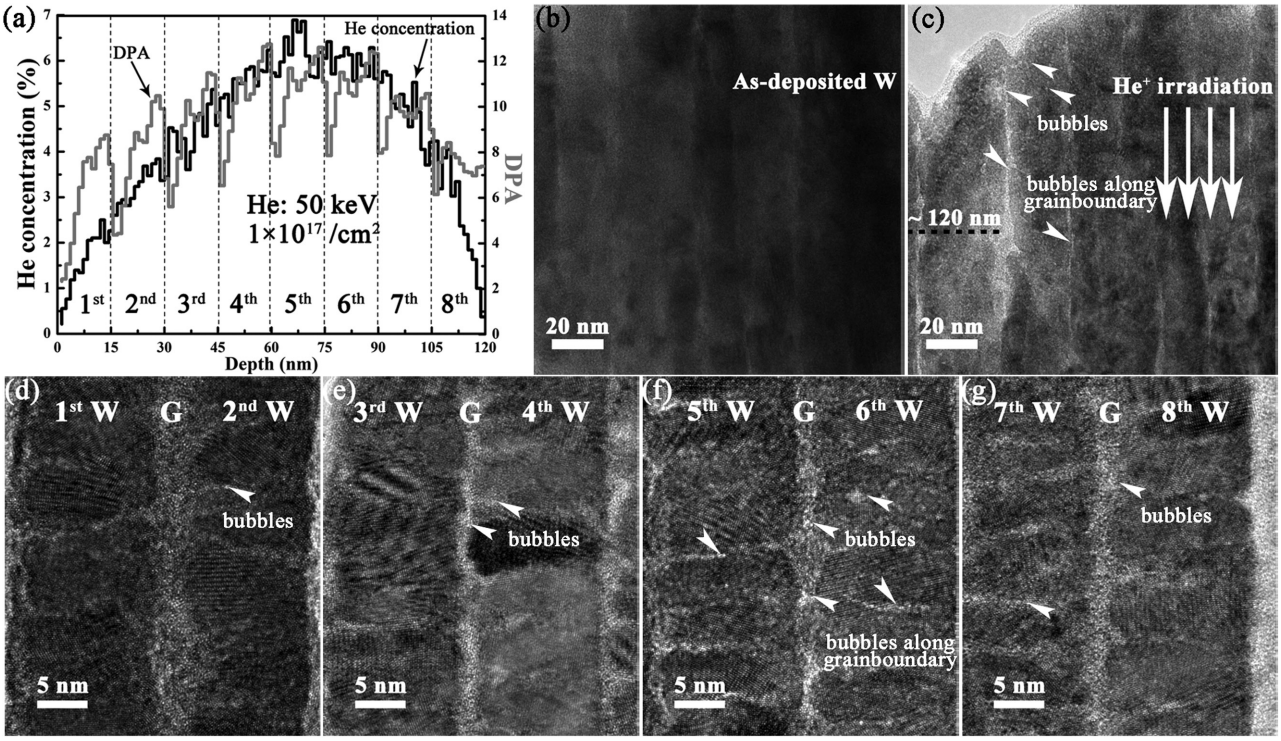

Figure 5. a) SRIM calculations that simulate the variation of He concentration (left) and DPA (right) versus radiation depth in multilayers with 15 nm period-thickness subjected to He^+-ions irradiation at 50 keV to a total influence of 1×10^{17} ions cm^{-2}, same as the experimental condition. b,c) TEM images: as-deposited W nanofilm (b); pure-W nanofilm (c) irradiated by 50 keV He^+ ions to a total influence of 1×10^{17} cm^{-2}. The black dashed line in (c) stands for the location underneath the film surface. (d)–(g) are TEM images of Figure 1 in different areas at high magnification, which correspond the marked location in (a).

in Figure 5a. TEM images of irradiated pure W nanofilm and W_{15}/G in different regions at the fluence of 5×10^{16} ions cm^{-2} are shown in Figure S6b–f (Supporting Information), and corresponding SRIM simulation of W_{15}/G is displayed in Figure S6a (Supporting Information). Figure 5d which is close to the surface shows that few He bubbles are formed. With the increase of implantation depth, the He bubble density increases and the W/G interfaces or grain boundaries become preferred locations for bubble formation. In an area of ≈60 nm underneath the film surface (Figure 5f), some He bubbles are clearly observed and a few bubbles are aligned and distributed along grain boundaries. It is worth mentioning that large areas of He bubbles are not clearly observed at the fluence of 5×10^{16} ions cm^{-2}. In addition, with the increase of He-ion concentration, He nanochannels gradually appear and reach up to the maximum quantity in the peak concentration area (Figure 5d–f). Also, in contrast to the W_{15}/G nanofilm, the irradiated pure W film has the most He nanochannels, which extend dozens of nanometers along the direction of implantation. Then, in the area close to the end of He-concentration profile, the number of He bubbles and He nanochannels tends to decline (Figure 5g). The results show that the higher the He concentration, the more He nanochannels appear to be formed for different locations of W_{15}/G multilayer nanofilm.

In summary, we fabricate W-graphene multilayer composites with period-thicknesses of 15, 30, and 40 nm. PT technique is used to characterize thermal transport across thin films. The calculated thermal resistance induced by the graphene layers sandwiched in tungsten films is under 1.8×10^{-8} K m^2 W^{-1}, which indicates that the reduction in thermal transport performance is moderate. Radiation tolerance is demonstrated by using a 50 keV He^+-ion irradiation to fluences of 5×10^{16} and 1×10^{17} ions cm^{-2}, respectively. The performances of the pure W nanofilms, as well as of several W/G and W/W multilayer nanofilms with different tungsten period-thicknesses of 15, 30, and 40 nm, are investigated and analyzed by means of TEM. Graphene inserted among the W films plays a dominant role in reducing radiation damage, especially in enhancing interface stability. It is much easier for the pure W nanofilm to form He bubbles than the W-graphene multilayered composites for He^+ irradiation. What is more, the smaller-period-thickness nanofilm exhibits higher radiation tolerance in the reduction of He-bubble density. All these results can enable us to design a promising structural material with both excellent thermal properties and radiation tolerance, which has great potential for radiation tolerance materials.

Experimental Section

Fabrication of Samples: The W/G multilayer composites were fabricated by alternately depositing tungsten film and transferring monolayer graphene. Monolayer graphene films were fabricated by modified chemical vapor deposition (CVD).[48] The fabrication process of W/G multilayer composites is shown as follows: first, the tungsten nanofilm was deposited on Si/SiO_2 (300 nm) in an ultrahigh vacuum magnetron sputtering system at room temperature. Then, the monolayer

graphene was transferred onto the surface of the tungsten film by a poly(methyl methacrylate) (PMMA) method.[48–50] Subsequently, the next W nanofilm with the same thickness was deposited on top of graphene. Finally, by repeating the above process, the W/G multilayer films could be obtained. Meanwhile, we designed three tungsten period-thicknesses: 15, 30, and 40 nm, as well as W/W multilayer films, which differed mainly in that no graphene transferred among the W layers. In addition, corresponding to these samples, a series of single-layer tungsten films were sputtered, which were similar to the multilayer films in total thicknesses. The detailed information is shown in the Supporting Information.

Helium-Ion-Beam Irradiation: Helium-ion implantation was performed, respectively, at room temperature with 50 keV to two fluences (5×10^{16} and 1×10^{17} ions cm^{-2}) using an ion implanter (LC22-100-01) at the Center for Ion Beam Application, Wuhan University. The SRIM computer program was used to calculate the DPA and He concentration versus radiation depth.

TEM-Sample Preparation: The TEM specimens were prepared by the conventional method. Gatan M-bond 610 epoxy was used to mount the sample between two Si wafers. Then, the sample was manually polished to ≈40 µm. Finally, dimpling is performed followed by Ar^+ milling with a voltage of 3 keV or lower to avoid ion-milling damage. TEM was performed on a Tecnai G2 F20 (FEI) microscope operated at 200 kV.

Supporting Information

Supporting Information is available from the Wiley Online Library or from the author.

Acknowledgements

S.S., W.L., and X.Z. contributed equally to this work. The authors thank the Professor Jianghua Chen, Professor Limei Cha, and Doctor Xiubo Yang of Hunan University for the support of TEM measurements. The authors acknowledge the NSFC (51371131, 11375134, 51571153, 51428603, and 51576145), Jiangsu Provincial Natural Science Foundation (BK20141217), and the Fundamental Research Funds for the Central Universities (2042015kf1012).

Received: August 29, 2016
Revised: September 22, 2016
Published online: November 17, 2016

[1] J. Knaster, A. Moeslang, T. Muroga, *Nat. Phys.* **2016**, *12*, 424.
[2] S. J. Zinkle, *Phys. Plasmas* **2005**, *12*, 058101.
[3] H. Trinkaus, B. N. Singh, *J. Nucl. Mater.* **2003**, *323*, 229.
[4] S. J. Zinkle, G. S. Was, *Acta Mater.* **2013**, *61*, 735.
[5] R. Cheaito, C. S. Gorham, A. Misra, K. Hattar, P. E. Hopkins, *J. Mater. Res.* **2015**, *30*, 1403.
[6] Z. Su'ud, R. Anshari, *AIP Conf. Proc.* **2012**, *1448*, 315.
[7] K. L. Murty, I. Charit, *J. Nucl. Mater.* **2008**, *383*, 189.
[8] S. J. Zinkle, J. T. Busby, *Mater. Today* **2009**, *12*, 12.
[9] G. Ackland, *Science* **2010**, *327*, 1587.
[10] H. L. Heinisch, F. Gao, R. J. Kurtz, *J. Nucl. Mater.* **2004**, *329*, 924.
[11] M. Zhernenkov, S. Gill, V. Stanic, E. DiMasi, K. Kisslinger, J. K. Baldwin, A. Misra, M. J. Demkowicz, L. Ecker, *Appl. Phys. Lett.* **2014**, *104*, 241906.
[12] X. Zhang, E. G. Fu, N. Li, A. Misra, Y. Q. Wang, L. Shao, H. Wang, *J. Eng. Mater. Technol.* **2012**, *134*, 041010.
[13] S. M. Mao, S. P. Shu, J. Zhou, R. S. Averback, S. J. Dillon, *Acta Mater.* **2015**, *82*, 328.
[14] Y. Gao, T. Yang, J. Xue, S. Yan, S. Zhou, Y. Wang, D. T. K. Kwok, P. K. Chu, Y. Zhang, *J. Nucl. Mater.* **2011**, *413*, 11.
[15] M. Callisti, M. Karlik, T. Polcar, *J. Nucl. Mater.* **2016**, *473*, 18.
[16] X. Zhang, N. Li, O. Anderoglu, H. Wang, J. G. Swadener, T. Höchbauer, A. Misra, R. G. Hoagland, *Nucl. Instrum. Methods Phys. Res., Sect B* **2007**, *261*, 1129.
[17] T. Höchbauer, A. Misra, K. Hattar, R. G. Hoagland, *J. Appl. Phys.* **2005**, *98*, 123516.
[18] E. G. Fu, J. Carter, G. Swadener, A. Misra, L. Shao, H. Wang, X. Zhang, *J. Nucl. Mater.* **2009**, *385*, 629.
[19] M. J. Demkowicz, D. Bhattacharyya, I. Usov, Y. Q. Wang, M. Nastasi, A. Misra, *Appl. Phys. Lett.* **2010**, *97*, 161903.
[20] Y. Chen, E. Fu, K. Yu, M. Song, Y. Liu, Y. Wang, H. Wang, X. Zhang, *J. Mater. Res.* **2015**, *30*, 1300.
[21] Y. Kim, J. Baek, S. Kim, S. Kim, S. Ryu, S. Jeon, S. M. Han, *Sci. Rep.* **2016**, *6*, 24785.
[22] E. T. Swartz, R. O. Pohl, *Rev. Mod. Phys.* **1989**, *61*, 605.
[23] A. A. Balandin, S. Ghosh, W. Z. Bao, I. Calizo, D. Teweldebrhan, F. Miao, C. N. Lau, *Nano Lett.* **2008**, *8*, 902.
[24] A. A. Balandin, *Nat. Mater.* **2011**, *10*, 569.
[25] C. Zhang, W. Zhao, K. Bi, J. Ma, J. Wang, Z. Ni, Z. Ni, Y. Chen, *Carbon* **2013**, *64*, 61.
[26] J. S. Bunch, S. S. Verbridge, J. S. Alden, A. M. van der Zande, J. M. Parpia, H. G. Craighead, P. L. McEuen, *Nano Lett.* **2008**, *8*, 2458.
[27] W. Ren, H. M. Cheng, *Nat. Nanotechnol.* **2014**, *9*, 726.
[28] X. Xu, Z. Zhang, L. Qiu, J. Zhuang, L. Zhang, H. Wang, C. Liao, H. Song, R. Qiao, P. Gao, Z. Hu, L. Liao, Z. Liao, D. Yu, E. Wang, F. Ding, H. Peng, K. Liu, *Nat. Nanotechnol.* **2016**, *11*, 930.
[29] L. Pentecoste, P. Brault, A. L. Thomann, P. Desgardin, T. Lecas, T. Belhabib, M. F. Barthe, T. Sauvage, *J. Nucl. Mater.* **2016**, *470*, 44.
[30] A. Hasegawa, M. Fukuda, K. Yabuuchi, S. Nogami, *J. Nucl. Mater.* **2016**, *471*, 175.
[31] G. Janeschitz, *J. Nucl. Mater.* **2001**, *290–293*, 1.
[32] H. Bolt, V. Barabash, W. Krauss, J. Linke, R. Neu, S. Suzuki, N. Yoshida, A. U. Team, *J. Nucl. Mater.* **2004**, *329–333*, 66.
[33] X. W. Wang, Z. R. Zhong, J. Xu, *J. Appl. Phys.* **2005**, *97*, 5.
[34] T. Wang, X. Wang, Y. Zhang, L. Liu, L. Xu, Y. Liu, L. Zhang, Z. Luo, K. Cen, *J. Appl. Phys.* **2008**, *104*, 013528.
[35] X. W. Chen, Y. P. He, Y. P. Zhao, X. W. Wang, *Nanotechnology* **2010**, *21*, 8.
[36] J. F. Ziegler, M. D. Ziegler, J. P. Biersack, *Nucl. Instrum. Methods Phys. Res., Sect B* **2010**, *268*, 1818.
[37] R. E. Stoller, M. B. Toloczko, G. S. Was, A. G. Certain, S. Dwaraknath, F. A. Garner, *Nucl. Instrum. Methods Phys. Res., Sect B* **2013**, *310*, 75.
[38] H. Hu, X. Wang, X. Xu, *J. Appl. Phys.* **1999**, *86*, 3953.
[39] Z. Chen, W. Jang, W. Bao, C. N. Lau, C. Dames, *Appl. Phys. Lett.* **2009**, *95*, 161910.
[40] Y. Yue, J. Zhang, X. Wang, *Small* **2011**, *7*, 3324.
[41] K. F. Mak, C. H. Lui, T. F. Heinz, *Appl. Phys. Lett.* **2010**, *97*, 221904.
[42] Y. K. Koh, M. H. Bae, D. G. Cahill, E. Pop, *Nano Lett.* **2010**, *10*, 4363.
[43] Y. Yue, J. Zhang, X. Tang, S. Xu, X. Wang, *Nanotechnol. Rev.* **2015**, *4*, 533.
[44] K. Jagannadham, *J. Vac. Sci. Technol. A* **2014**, *32*, 051101.
[45] G. A. Slack, *Phys. Rev.* **1962**, *127*, 694.
[46] D. Kiener, P. Hosemann, S. A. Maloy, A. M. Minor, *Nat. Mater.* **2011**, *10*, 608.
[47] H. Huang, X. Tang, F. Chen, Y. Yang, J. Liu, H. Li, D. Chen, *J. Nucl. Mater.* **2015**, *460*, 16.
[48] X. Li, W. Cai, J. An, S. Kim, J. Nah, D. Yang, R. Piner, A. Velamakanni, I. Jung, E. Tutuc, S. K. Banerjee, L. Colombo, R. S. Ruoff, *Science* **2009**, *324*, 1312.
[49] L. Jiao, B. Fan, X. Xian, Z. Wu, J. Zhang, Z. Liu, *J. Am. Chem. Soc.* **2008**, *130*, 12612.
[50] K. S. Kim, Y. Zhao, H. Jang, S. Y. Lee, J. M. Kim, K. S. Kim, J. H. Ahn, P. Kim, J. Y. Choi, B. H. Hong, *Nature* **2009**, *457*, 706.